Supplementary/supporting information

1. Refinement of hexagonal phase

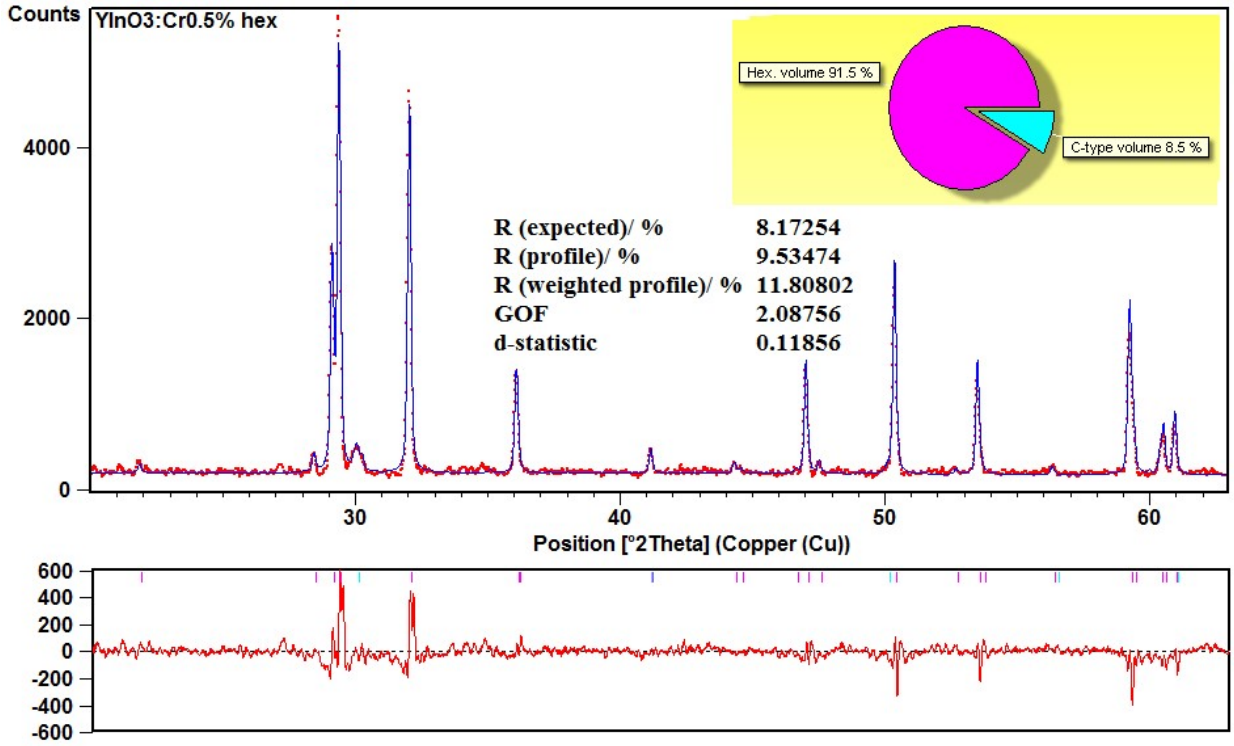

Figure 1S HighScore Rietveld refinement of hexagonal Cr^{3+}-doped $YInO_3$.

2. The visible absorption/excitation and emission

In the F(R) absorption spectra (Figure 5a), some features were observed in the visible range after 370 nm. This allowed analyze in particular visible absorption/excitation and emission spectra of hexagonal $YInO_3$:Cr^{3+} (Figure 2S). The measured excitation spectra were composed of three peaks with maxima at 18248, 21551, and 24510 cm^{-1} (408, 464, and 548 nm) attributed to the following transitions: $^4A_2 \rightarrow {}^4T_2$, $^4A_2 \rightarrow {}^2T_2$ and $^4A_2 \rightarrow {}^4T_1$, which are specific for Cr^{3+} dopant (Figure 2S, b). The excitation data were taken using emission energy of 14368 cm^{-1} (696 nm) specific for the $^2E \rightarrow {}^4A_2$ spin-forbidden transition. The shape of the excitation and emission curve is close to that reported for Cr^{3+}-doped $LaAlO_3$ perovskite phosphor with a particular shift in UV due to host difference [52]. Two dopant concentration were used with 0.5% and 1% of Cr^{3+} to confirm the emission shown in Figure 2S, b. Pumping separately in the three mentioned excitation peaks, the 408 nm gives the most intensive emission at 696 nm, as shown in Figure 2S, b inset.

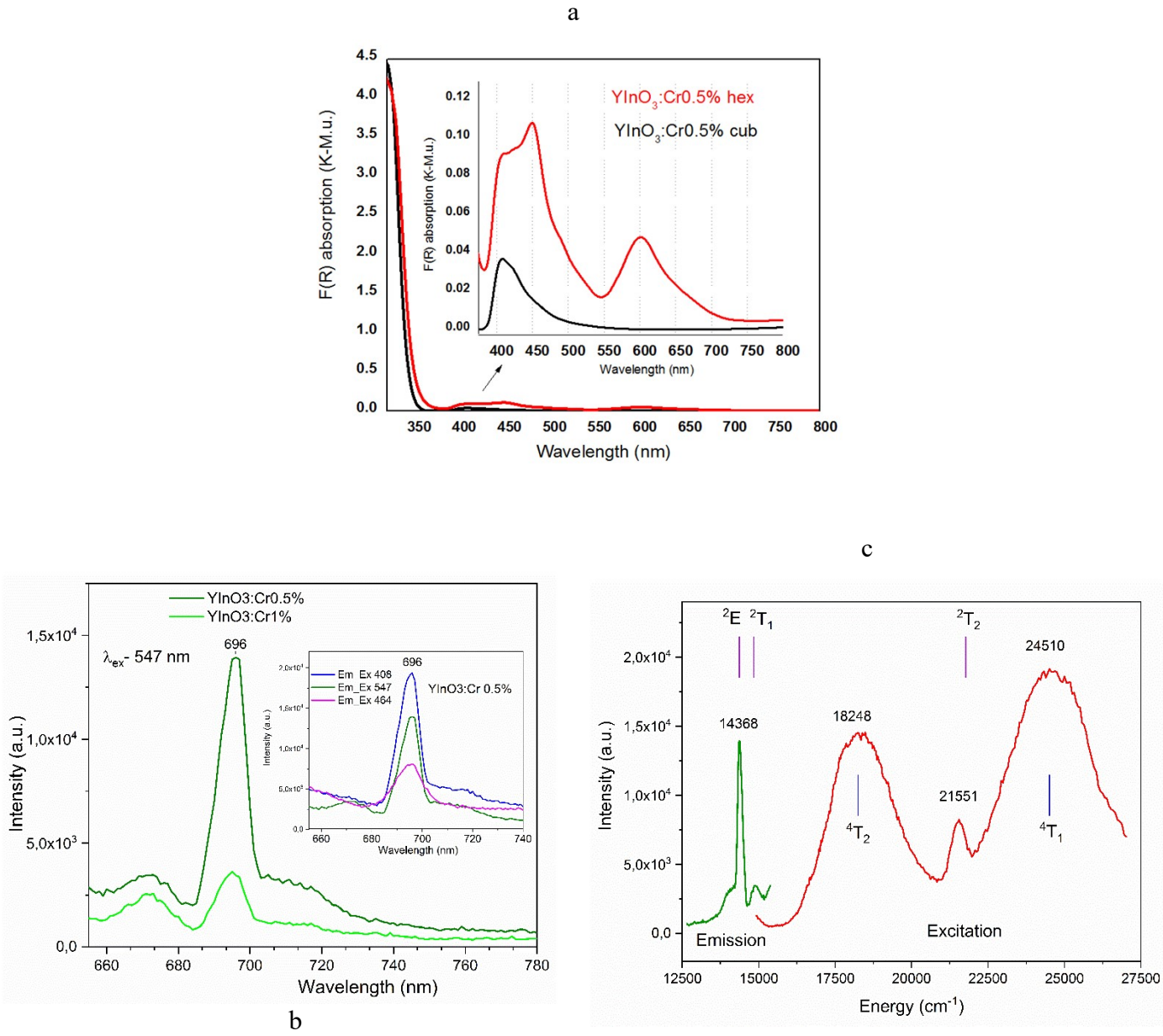

Figure 2S (a) Kubelka–Munk absorption spectra of both $YInO_3$ phases. (b) Photoluminescence emission spectra. (c, inset) Effect of excitation wavelength on the 696 nm emission. The calculated energy levels (vertical lines) corresponding to excitation and emission of the Cr^{3+} dopant in hexagonal $YInO_3$ are also shown.

Doping with the chromium ions may induce some distortion of the crystal lattice near the In^{3+} site (occupied by Cr^{3+}), to make one of the remote oxygen ions to move closer to form a quasi-6-fold coordination. We presume this is the case for hexagonal sample, because the consistent calculations of crystal field effects for the 5-fold coordination would not return a proper sequence of the Cr^{3+} energy levels.

To calculate the Cr^{3+} energy levels in this work, we used a simplified approach, getting the values of the crystal field strength *Dq*, Racah parameters *B*, *C* from the PLE/PL spectra. It is based on the following equations (derived from the Tanabe-Sugano matrices for the energy levels of the d^3 electron configuration) using the energies $E(^4T_{2g})$, $E(^4T_{1g}(^4F))$, and $E(^2E_g)$ of the $^4T_{2g}$, $^4T_{1g}(^4F)$, and ^2E_g states:

$$E\left(^4T_{2g}\right) = 10Dq \tag{1}$$

$$\frac{B}{Dq} = \frac{\left(\frac{\Delta E}{Dq}\right)^2 - 10\left(\frac{\Delta E}{Dq}\right)}{15\left(\frac{\Delta E}{Dq} - 8\right)} \tag{2}$$

$$\frac{E\left(^2E_g\right)}{B} = \frac{3.05C}{B} + 7.90 - \frac{1.80B}{Dq} \tag{3}$$

where $\Delta E = E(^4T_{1g}(^4F)) - E(^4T_{2g})$ [29].

The obtained values (in cm^{-1}) are typical for the octahedral Cr^{3+} ions and are *Dq*=1825, *B*=600, *C*=3273. Using these values, we calculated the remaining energy levels from the Tanabe-Sugano matrices for the d^3 electron configuration and superimposed them on the spectra, as shown by the vertical lines in Figure 2Sa. There is a good agreement between the spectra and calculated energy levels, even the peak at 21551 cm^{-1} agrees well with the $^2T_2$ level.

3. VUV mapping and potential defects

As it was mentioned synchrotron-based VUV radiation enables a substantial extension of the luminescence excitation energy range, well beyond the energy of the $^4T_1$ transition (Figure 3S). Under VUV excitation, the extensive excitation–emission maps were recorded in both VIS and NIR spectral regions. Figure 3S, presents the results obtained for $YInO_3:Cr^{3+}$ (0.5%) with hexagonal and cubic crystal structures. Several cross-sections are simultaneously displayed on the excitation–emission maps to illustrate the corresponding excitation and emission spectra. As it was mentioned the observed luminescence spectra originate from excitation of the host lattice followed by subsequent energy transfer to the luminescent centers.

In the case of hexagonal $YinO_3:Cr^{3+}$, the defect-related luminescence is more complex, and its spectral position exhibits a pronounced dependence on the excitation energy (Figure 3S, a). Under low-energy excitation (325–300 nm), the defect band shows an emission maximum at approximately 540 nm. However, when the excitation wavelength is reduced below 280 nm, this

band undergoes a pronounced blue shift, with an emission maximum around 480 nm. In this excitation regime, the observed band closely resembles that detected for the cubic-phase sample (Figure 3S. b). Furthermore, when the excitation wavelength becomes shorter than 200 nm, an additional luminescence band emerges with a maximum near 400 nm. Notably, the excitation spectrum of this high-energy band differs radically from those of the other bands, exhibiting a well-defined threshold and clearly resolved excitation bands at 176 and 153 nm (Figure 3S, a). These two features are also visible in the excitation spectrum of the cubic $YinO_3:Cr^{3+}$ as small peaks superimposed on a broad, structureless band (Figure 3S, b).

In the cubic $YInO_3$, this intense broad emission has two components: a peak at 481 nm and a shoulder at 510 nm. The former could be attributed to charge transfer band (CTB) emission, being also reported as 350-550 nm broad emission under 256 nm excitation [5]. The latter were attributed to oxygen related defects/vacancies by Shukla et al in a similar host or by I. Chatratin in pure cubic In_2O_3 host with emission at 2.3 eV (538 nm)[5,53]. A pronounced increase in the excitation spectrum, observed in the 325–280 nm range (Figure 3S,b), can be attributed to interband CTB from $O^{-2} \rightarrow Cr^{3+}$ transitions similar with the reported absorption band 220-280 nm in C-type $YInO_3$ [5]. Such strong absorption in the range 350-450 nm was also observed in In_2O_3 samples, and when doped with Cr^{3+} the intensity of the band increase [54]. At shorter wavelengths, the excitation spectrum reflects the density of electronic states in the conduction band.

As noted earlier, the bandgap of $YinO_3:Cr^{3+}$ is of 3.6 eV. Consequently, the absorption coefficient at such excitation energies is very high, resulting in an extremely small penetration depth of the incident radiation. Under these conditions, mainly the surface regions of the nanoparticles are excited. It is well known that oxide nanoparticle surfaces host a large number of structural and electronic defects. Moreover, the reduced particle size and high surface-to-volume ratio observed by SEM are consistent with the pronounced contribution of luminescence under UV/VUV excitation. Therefore, we attribute the broad luminescence bands observed in Figure 3S (a, b) to surface-related defect states. In the cubic modification, a single dominant defect type is likely responsible for the emission, whereas in the hexagonal structure two or more defect types appear to be involved, leading to a more complex spectral behavior. It is also worth highlighting the shortest-wavelength luminescence observed in the hexagonal sample (Figure 3S, a).

The fact that this emission exhibits an excitation threshold significantly higher than the bandgap of $YInO_3$ suggests that an additional crystalline phase may be present at the particle surface. This value closely matches the excitation threshold of the high-energy emission band in the hexagonal sample, supporting the hypothesis that thin surface layers or nanoscopic inclusions of Y_2O_3 contribute to the observed short-wavelength luminescence. It should be noted that such a surface phase may remain undetectable by conventional X-ray diffraction techniques due to its very low concentration. Luminescence spectroscopy, however, is significantly more sensitive to local structural and electronic environments and is therefore capable of revealing even extremely weak contributions from minority surface phases.

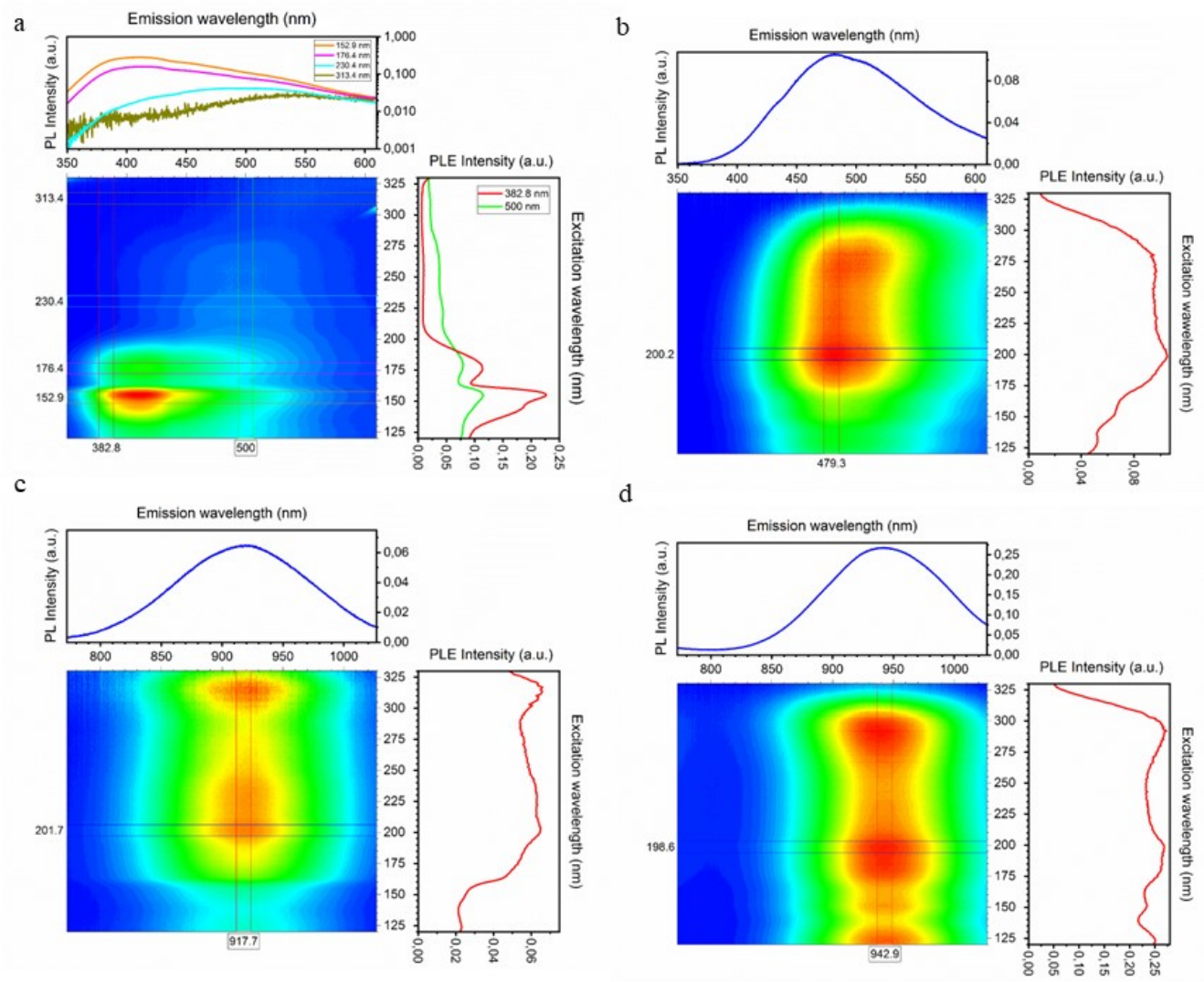

Figure 3S. Excitation-emission maps for hexagonal (a, c) and cubic (b, d) $YInO_3:Cr^{3+}$

Since this emission appears exclusively in Cr-doped samples, it is reasonable to assign it to NIR transitions within Cr^{3+} ions. Yet the obvious question is why this UV/VUV-induced broad luminescence differs from the narrow 696 nm, Cr^{3+} line observed under visible excitation (Figure 2S). This difference can be rationalized by considering both the Tanabe–Sugano framework for d^3 ions and the fact that UV/VUV excitation interacts predominantly with the near-surface region of the particles. Under visible excitation, low-energy intra-configurational $^4A_2 \rightarrow {}^4T_2/{}^4T_1$ transitions are selectively excited in Cr^{3+} ions residing in regular octahedral lattice sites. In these bulk-like environments, the crystal field is relatively strong, allowing efficient relaxation into the ^2E state, which becomes the lowest excited state in the strong-field limit. The subsequent spin-forbidden $^2E \rightarrow {}^4A_2$ transition gives rise to the characteristic narrow R-line emission observed in Figure 2S.

An additional argument supporting the assignment of the NIR emission to surface Cr^{3+} ions is the strong similarity between the excitation spectra of this emission and those of defect-related luminescence. This indicates that UV/VUV excitation triggers a surface-driven process in which

absorption within a very thin surface layer generates carriers that are promptly trapped by surface defect states, and the energy stored in these defect-related excitations is subsequently transferred to nearby surface Cr^{3+} ions. This sequence of events naturally explains why the NIR emission originates from surface Cr^{3+} centers rather than from Cr^{3+} ions located in the interior of the particles of hexagonal $YInO_3$ host.